

Chapter 17

Nanotribological Studies by Nanoparticle Manipulation

Dirk Dietzel, Udo D. Schwarz and André Schirmeisen

Abstract Friction of extended nanocontacts has lately become a subject of growing interest in nanotribology. The related length scales, which are not accessible to conventional friction force microscopy, can best be analyzed by measuring the friction of nanoparticles sliding over flat surfaces. By pushing nanoparticles with an AFM tip a large range of materials combinations and contact areas can be studied under well-defined interface conditions, therefore offering new insight into atomistic concepts of friction.

17.1 Nanoparticle Manipulation: An Alternative Route to Nanotribology

Since its invention in 1987, friction force microscopy (FFM) [1] has become a widespread technique for the investigation of frictional processes. By detecting the lateral forces acting between the tip of an atomic force microscope (AFM) and the sample surface, this technique has proven to be a versatile tool for the analysis of a wide variety of nanoscale frictional phenomena [2, 3].

In conventional FFM operation, the lateral force signal, which is proportional to the friction-induced cantilever torsion, is recorded during the sliding of the cantilever across the surface. The lateral force therefore originates from the contact between tip and surface. Measurements have been performed as a function of a wide variety of parameters such as the externally applied cantilever load [4–9], radius and shape of the AFM tip [4, 6, 7], sliding velocity [10–13], the temperature [14–16], the relative orientation between scan direction and substrate lattice [17–20], or the chemical nature of the sample [21–23]. Often, FFM studies led to the successful analysis of frictional processes at the atomic scale [1, 10, 13, 16].

D. Dietzel · A. Schirmeisen (✉)
Institute of Applied Physics (IAP), Justus-Liebig-Universität, Giessen, Germany
e-mail: schirmeisen@uni-giessen.de

U.D. Schwarz
Department of Mechanical Engineering and Materials Science and Center for Research on Structures and Phenomena (CRISP), Yale University, New Haven, CT, USA

But despite the indisputable successes of many FFM studies, this method still has severe inherent limitations. Mainly four aspects are of concern.

1. While the nature of the samples can be freely selected, commercially available AFM tips are usually limited to a very narrow set of materials, mostly silicon, silicon oxide, silicon nitride, and diamond. This limits the number of material combinations that can be investigated. To overcome that limitation, other materials can be evaporated onto AFM cantilevers. This strategy, however, generally leads to AFM tips of inferior quality and/or unknown geometry unless performed in a very controlled way. In addition, many materials that are applied as thin films to cover the AFM tip will wear out fast due to the significant shear stresses during scanning.
2. AFM tips used for FFM generally feature amorphous or disordered tip ends. Therefore, it is very difficult to investigate the effect of ordered structures on friction, which is expected to have a dramatic influence under certain circumstances. Most prominently, an effect denoted as *superlubricity* [24] or, more precisely, *structural lubricity* [25] is expected to occur at specific relative orientations of extended atomically flat contacts that show crystalline long-range order [26–29].
3. Related to the above point is the question how friction depends on the ‘true’ contact area at the atomic scale. It can be argued that the contact area dependence of friction is one of the most fundamental yet unsolved issues in nanotribology, as its understanding is crucial for successfully bridging the conceptual gap between nanoscale and microscale friction. Unfortunately, the fixed tip radius of commercially available cantilevers makes it difficult to analyze effects as a function of the contact area. This leaves a ‘gap’ in the experimental accessibility of contact areas between the tens of nm² realized in FFMs and the typically ten thousands of μm² found in surface force apparatus measurements [30, 31]. In addition, the determination of the contact area has to rely on the realization of a specific contact geometry (usually the Hertzian contact geometry, representing a spherical tip apex on a flat surface) and on the validity of certain assumptions of the contact mechanical models [32].
4. Recent theoretical studies also indicate that the contact area is not necessarily a sufficient parameter to describe the geometry of the interface [33]. The shape of the interface can influence friction as well, meaning that two nanoscopic contacts of same size but different shape can show decidedly different friction. And while some attempts have been made to analyze the contact area of friction experimentally [6, 7, 34, 35], so far there are no experimental studies related to the shape of the contact area.

In order to overcome these limitations, it would be desirable to have a method available that measures the interfacial friction of structurally well-defined contacts of arbitrary sizes, shapes, and material combinations. One possible solution is to use the AFM tip as a manipulation tool for controlled lateral manipulation of nanoscale particles supported by flat substrates [36] (see Fig. 17.1).

The concept of nanoparticle manipulation was first demonstrated with the example of C₆₀ islands grown on a NaCl surface [37] and later used to investigate frictional

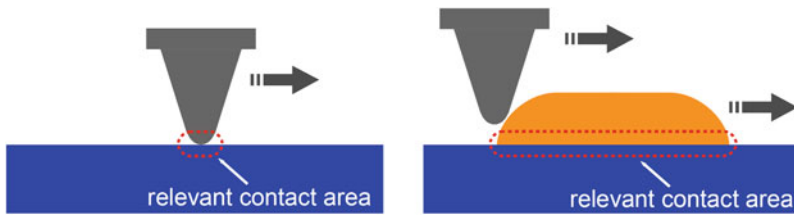


Fig. 17.1 The difference between conventional friction force microscopy studies and particle manipulation schemes lies in the relevant interface. While FFM is limited to friction occurring at the interface between tip and surface (*left*), the particle manipulation method allows to study the much larger, but well-defined particle/surface interface (*right*)

anisotropies for MoO nanoparticles [38]. Nanoscale objects, like nanotubes, have been pushed to distinguish sliding and rolling motion [39]. Recently, there has been an increase of systematic friction studies using nanoparticle manipulation, highlighting the influence of surface structure on particle trajectories [40] as well as the influence of parameters like surface chemistry and temperature [41]. The influence of relative orientation between particles, substrate, and direction of manipulation was analyzed for ligand-capped CdSe nanorods [42]. The fundamental question of how friction is related to contact area has been addressed by a systematic variation of the size of metallic nanoparticles [34, 35]. Furthermore, nanoparticle manipulation experiments have been used to analyze the difference between static and sliding friction. While some experimental approaches are mainly sensitive to either static friction [34, 43] or sliding friction [35], recent experiments have demonstrated, how nanoparticle manipulation can be used to monitor the transition from static to sliding friction [44].

The range of contact areas that is accessible to nanoparticle manipulation experiments is indicated in Fig. 17.2 in comparison to other experimental tools commonly used in nano- and microtribology, namely the friction force microscope (either with

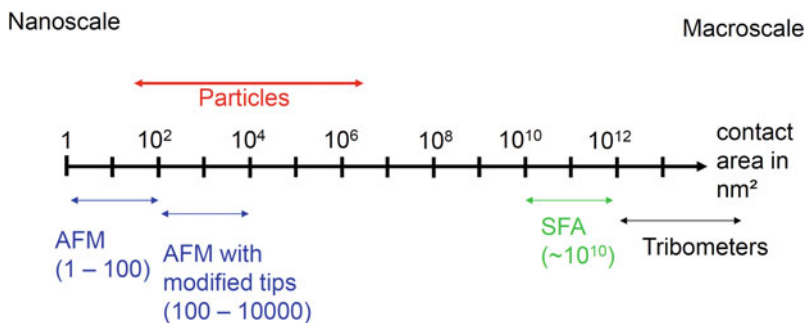


Fig. 17.2 Overview over the different ranges of contact areas covered by tribological techniques on the nano- and meso-scale

standard or modified tips) [1, 6, 7, 10], the surface force apparatus [45, 46], and the quartz crystal microbalance (QCM) [47–49]. As Fig. 17.2 illustrates, nanoparticle manipulation offers unique access to lengthscales at the transition between the nano- and meso-scale.

17.2 Friction Measurements by Nanoparticle Manipulation: Experimental Approach

Since the sharp tip of an atomic force microscope is an ideal tool to push nano-objects on a surface, the AFM has become the common basis for all nanoparticle manipulation schemes. For conventional topography measurements, an AFM is typically operated in two main modes: In the *contact* (or static) *mode* tip and sample are in direct mechanical contact. This technique can be used to obtain nanometer resolution images on a wide variety of surfaces. Higher resolution, however, is often achieved using dynamic modes like tapping mode [50], or noncontact mode [51], where the cantilever oscillates near the sample surface. For both the contact and the dynamic mode, it has been shown, that they can be successfully applied to facilitate nanoparticle sliding with simultaneous assessment of energy dissipation. The resulting different experimental approaches to nanoparticle manipulation are described in the following subsections.

17.2.1 Dynamic AFM Techniques for Nanoparticle Manipulation

In the dynamic mode, the cantilever is typically oscillated close to its resonance frequency while the oscillation amplitude serves as feedback parameter. The energy that is dissipated during one oscillation cycle ΔE is then a function of cantilever spring constant c_z , the quality factor Q , and the drive and oscillation amplitudes a_d and A , respectively [52]:

$$\Delta E = \pi c_z \left(A a_d \sin(\phi) - \frac{A^2 f_d}{Q f_0} \right). \quad (17.1)$$

Here, f_d and f_0 are the driving and oscillation frequencies and ϕ is the phase shift between them. Controlled manipulation of latex spheres on highly oriented pyrolytic graphite (HOPG) substrates in the dynamic mode was demonstrated by Ritter et al. [53]. Basically, when the oscillating tip hits the rim of the nanoparticle, energy is transferred causing a lateral movement of the particle. The efficiency of this process is determined, among other factors, by the a priori unknown impact angle (see Fig. 17.3). For controlled manipulation, the tip is placed at the side of the particle and the oscillation amplitude is increased until particle motion is observed.

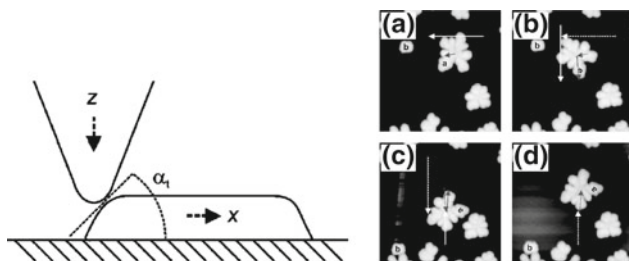


Fig. 17.3 *Left* Sketch of the tip-particle coupling. The impact angle at between tip and antimony particle determines the normal (z) and lateral (x) components of the acting force. *Right* Illustration of the dynamic mode manipulation procedure for Sb on HOPG (image size $1 \times 1 \mu\text{m}^2$). **a** Overview of the particle of interest (labeled with a) and the surrounding area. A white and a gray arrow indicate the path of the subsequent tip motion and the resulting dislocation of the particle, respectively. **b** Topography after the manipulation, showing a lateral translation of 83 nm and an in-plane rotation of 58° . **c** Result of the second manipulation step, and **d** final result after the third manipulation step (adapted from [34])

The particles can be translated when the power input exceeds a threshold value necessary to overcome the friction force of the adsorbed particle. By changing the amplitude of the dither piezo that drives the cantilever oscillations while the feedback loop is continuously working, it is possible to switch between an imaging mode and a manipulation mode with variable power input into the sample. Thus, an individual adaptation to the sample properties is feasible.

In the case of a free cantilever, increasing the amplitude of the dither piezo leads to an increase of the effective oscillation amplitude, which scales linearly with the excitation. During the manipulation experiments, however, the excitation is increased when the cantilever is still in feedback. The feedback system tries to maintain the preselected setpoint amplitude of the cantilever by decreasing the distance between cantilever and sample. Recording the dither amplitude, the setpoint, and the phase angle allows one to calculate the power dissipation during manipulation by using (17.1). Theoretical analysis shows that this value is in fact a measure of the lateral forces occurring during manipulation [54].

The dynamic mode is characterized by a very high degree of flexibility, since particle motion in arbitrary directions can be performed. Furthermore, the range of lateral forces that can be applied to the particle for translation is related to the square of the oscillation amplitude, which yields a very large dynamic range. The excitation amplitude can indeed be adjusted over orders of magnitude, if necessary, to switch between gentle imaging and manipulation of even the biggest particles.

The above discussion shows that very controlled manipulation of individual particles is possible. For its successful realization, however, it is necessary to have an electronic AFM control system available, such as the one used to perform the particle manipulation shown in Fig. 17.3, where arbitrary tip motions along user-defined trajectories have been carried out under full feedback control. Unfortunately, this is often impossible with commercial AFM systems. A different approach relies on the

statistical movement of a large ensemble of particles of similar size. Mougín et al. [41] and Paolicelli et al. [43, 55] have systematically analyzed the amplitude threshold necessary to induce particle motion in dynamic mode during surface scanning. For gold nanoclusters deposited on.

Similarly, Gnecco et al. report a detailed analysis of particle trajectories due to the impact between the oscillating tip and the particle within one scan frame [40].

Unfortunately, the tapping mode, which has been commonly used for nanoparticle manipulations using tapping mode AFM operation, is not suitable for UHV conditions [51]. Instead, the frequency modulation mode (FM-AFM) must be used under UHV conditions. However, due to its self excitation principle, this mode is very sensitive against perturbations. Therefore, trying to manipulate typical nanoparticles with contact areas larger than a few 100 nm^2 will often result in the breakdown of cantilever oscillations, making this mode inapt for nanoparticle manipulations. However, it has been shown how the FM-AFM mode can be applied to move extremely small structures like single atoms [56] or PTCDA-molecules [57] with simultaneous assessment of the forces required to move the atoms or molecules.

17.2.2 Contact Mode AFM Techniques for Nanoparticle Manipulation

17.2.2.1 Pushing Nanoparticles from the Side

As an alternative to nanoparticle manipulation performed in tapping mode, manipulation can be carried out during contact mode operation [38, 39, 58–60]. The two most crucial parameters influencing the manipulation of the particles in contact mode are the stiffness of the cantilever and the component of the tip force exerted during the scan along the surface normal. As the cantilever stiffness is set once a particular cantilever has been chosen, the normal force represents the most important factor in the manipulation process. By increasing or decreasing the normal force, one can switch between imaging and manipulation in a controlled manner: If the normal force is below a certain threshold, the cantilever, which is always scanned with the feedback loop on, follows the topography of the sample. Only if the normal force is above the threshold, the feedback loop does no longer compensate for the height difference of the island, but rather pushes the island along with the cantilever. These two possible ways of interaction between cantilever, island, and substrate are depicted schematically in Fig. 17.4.

This manipulation technique was optimized by scanning with a constant normal force that is very close to the threshold of manipulation. An example for such manipulation is presented in Fig. 17.5, where the island is moved sideways during one particular scan line. Quantitative information can then be gained from the topography and friction signals acquired during the translation process (Fig. 17.7e). Essentially,

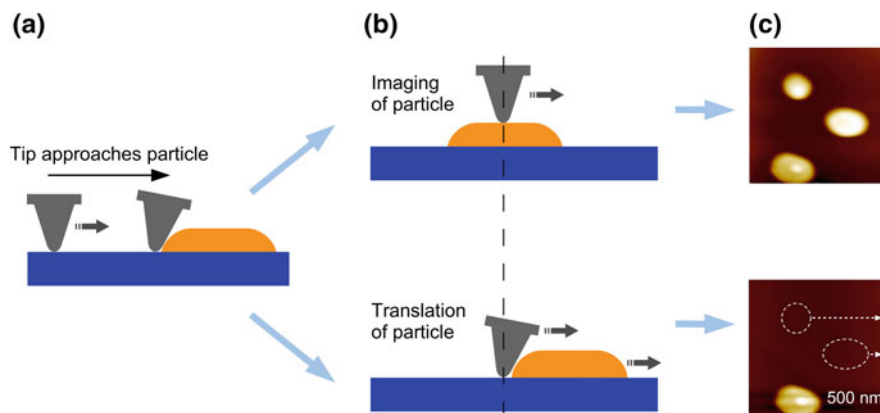


Fig. 17.4 Schematic representation of the two different interaction scenarios that might occur when the tip reaches a particle **a** Tip approaches the particle. In both subsequent scenarios, the tip will experience additional torsion once it reaches the rim of the particle. **b** *Top* if the normal force is below the dislocation threshold, the tip will trace the topography without moving the particle. The cantilever's additional torsion then represents the tip-particle friction on the island. *Bottom* if the dislocation threshold is exceeded, the feedback loop does not follow the topography but instead the tip will start pushing the particle. In this case, an additional lateral force corresponding to the particle-surface friction can be observed by monitoring the cantilever torsion. **c** Topography scans taken before and after the two upper particles were moved to the right

the sudden increase of the lateral force signal during the pushing process represents the friction of the manipulated island.

The main advantages of this manipulation approach is, that it allows to measure friction for a number of particles in a relatively short time, because often several displacements can be observed during an image. But since there is no way to precisely control the tip-particle interaction, it is often difficult to avoid unwanted nanoparticle motion. Thus, translation of a specific nanoparticle in a well defined way is challenging. In order to improve the manipulation procedure, the AFM can be operated in non-contact mode (either constant amplitude mode [51] or constant excitation mode [61, 62]) for recording topography images. From these images, a particle suitable for manipulation can be chosen and the tip can be positioned beside the nanoparticle, before switching back to contact mode. By moving the AFM tip along a straight pathway with a sufficiently high normal force, the nanoparticle can now be displaced, before the AFM is switched back to non-contact mode [60, 63]. The lateral force signal obtained during such a manipulation is found to be very similar to the shape shown in Fig. 17.5e).

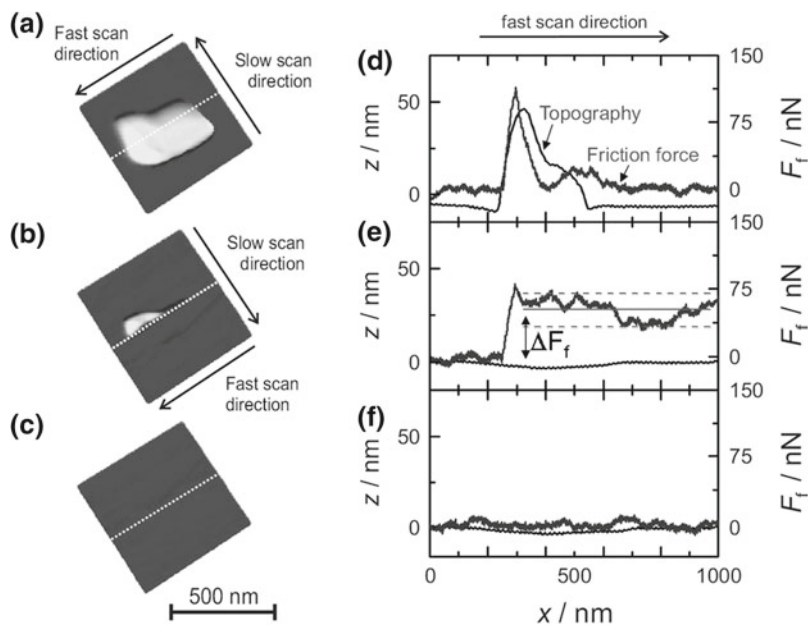


Fig. 17.5 Illustration of the particle manipulation procedure based on scanning with a constant normal force close to manipulation threshold. **a** Imaging of a nanoparticle at low external loading force. **b** A slight increase of the load initiates particle motion. The particle is imaged for several line scans before it is pushed out of the field of view (along the white dotted scan line), thus showing a 'cut' particle. **c** Surface image after translation, confirming that the particle has been moved out of the field of view. **d** Topography (left axis) and lateral force (right axis) of the last scan line before translation. The lateral force signal is mainly topography-induced, as the cantilever twists at the particle's edges. **e** Scan line during displacement. The topography now reflects the flat graphite surface, while the average frictional resistance of the particle can be determined from the lateral force signal. **f** First scan line after manipulation (adapted from [35])

17.2.2.2 Nanoparticle Trajectories During Manipulation

Ideally, when pushing a nanoparticle from the side, both the tip and the nanoparticle should move the same distance along a straight line. However, the shapes of tip and nanoparticle can lead to force components perpendicular to the tip path [40, 43], which can cause the contact between tip and nanoparticle to break. Once this happens, the AFM tip will continue its path but leave the nanoparticle behind. During nanomanipulation experiments, this effect can be minimized by trying to direct the tip trajectory through the center of mass of the nanoparticle. It can nonetheless be problematic with respect to the accuracy of particle positioning and, more importantly, it can also affect the friction force measured during the particle manipulation. For the simplest case of a round particle and a round tip, the geometrical configuration used to calculate the particle trajectory is depicted in Fig. 17.6. For the calculation of the particle trajectories it is assumed that any dependence of

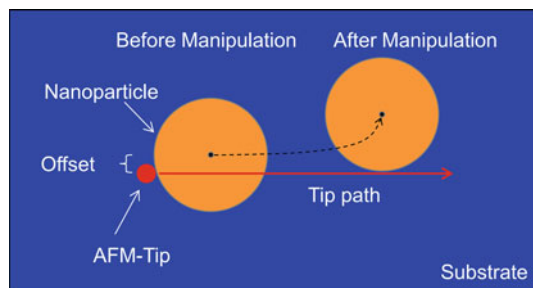


Fig. 17.6 Schematic of geometry during off-center manipulation. The position of the nanoparticle is shown in relation to the AFM-tip and the tip path directly before and after the manipulation takes place. The *dotted line* indicates the particle trajectory during manipulation. The most crucial parameter do describe the manipulation process is the offset between the AFM tip and the center of mass of the nanoparticle measured perpendicular to the tip path

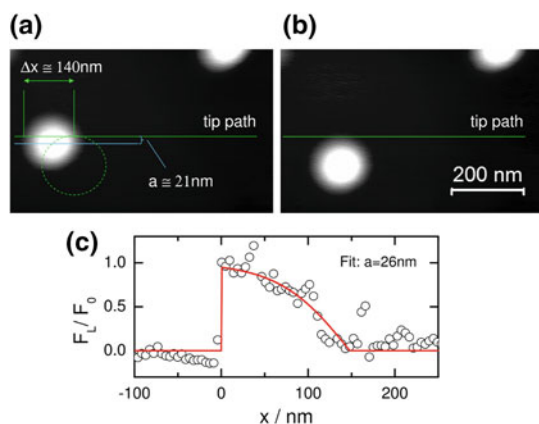


Fig. 17.7 Example of a manipulation event where the tip was moved from left to right and pushed an nanoparticle downwards during manipulation. **a** Topography image of the Sb nanoparticle on HOPG substrate before manipulation, **b** topography image after manipulation. The tip path and the position of the nanoparticle after manipulation are indicated in **(a)** and allow to estimate the offset $a \cong 21$ nm. **c** Lateral force signal measured during the manipulation. A fit to the experimental data yields $a = 26$ nm (image adapted from [63])

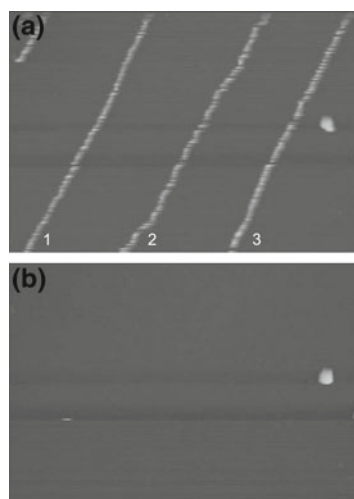
friction on sliding direction and sliding velocity can be neglected. Furthermore, the tip radius was assumed to be pointlike. The theoretical equations derived from this configuration [63] have subsequently been used to analyze the friction signal measured for an off center manipulation of an antimony nanoparticle on HOPG (see Fig. 17.7). In this experiment an antimony nanoparticle of about 150 nm diameter was pushed from the side by the AFM tip and after manipulation, a considerable displacement perpendicular to the tip path was found (Fig. 17.7a, b). The corresponding lateral force signal shows the typical steep increase, when the tip hits the nanoparticle, but starts to decrease immediately until the friction is back to the initial level after

approximately 150 nm, meaning that the tip has lost contact with the nanoparticle. This behaviour can be well fitted by a theoretical friction profile calculated for an offset a of 26 nm between nanoparticle and tip. From the AFM images measured before and after nanoparticle manipulation, the offset a can be estimated to 21 nm. Thus fit parameter and directly measured offset are in good agreement. If the lateral force signal can be described by a theoretical model, as shown in Fig. 17.7, the interfacial friction can still be precisely determined. However, such a calculations become increasingly complicated for more irregularly shaped particles and from a practical point of view, it is therefore preferably to limit any quantitative analysis to particle manipulations with straight trajectories.

In other experiments by Gnecco et al., the continuous off-center manipulation of nanoparticles during imaging has been used to force groups of nanoparticles onto common resulting trajectories, an approach which can be used for arranging nanoparticles on surfaces or for sorting of nanoparticles. In order to do so, Rao et al. have scanned a Si surface covered with a number of round colloidal gold nanoparticles in tapping mode, while the tip sample interaction was chosen to be well above the threshold of manipulation [40]. This way, whenever the AFM tip hits a nanoparticle, the nanoparticle is displaced according to a theory similar to the one used to describe contact mode measurements [40, 64]. Again, the determining factor is the offset between the tip path and the nanoparticles center of mass. Rao et al. have shown, that this parameter can be tuned by the line spacing during imaging and the nanoparticles can thereby be forced onto straight passes, where the effective angle of the trajectories is directly related to the line spacing (see Fig. 17.8).

Recently Nita et al. have applied the manipulation concept developed by Rao et al. to push antimony nanoparticles of complex shape by contact mode AFM techniques on MoS₂ [65], where the shape of the particles led to trajectories far more irregular,

Fig. 17.8 Topography images recorded in tapping mode during forward scan (a) and backward scan (b). The forward scan (a) shows three parallel trajectories of the gold nanospheres on a Si substrate. No trajectories are found in the backward scan (b), which means that the particles are efficiently pushed from the tip path during the forward scan and are not interacting with the tip during the backward scan (image taken from [64])



than the ones shown in Fig. 17.8a. However, by using the precise particle shape as input for numerical simulations, the particle trajectory could accurately be described and quantitative data for the interfacial friction was extracted [65]. These quantitative results obtained in contact mode hint toward a promising route of extracting friction from nanoparticles manipulations, since simple a imaging procedure, as it is possible with even very basic AFMs, allows to record data, from which friction values can be obtained.

17.2.2.3 ‘Tip-on-Top’-Approach

A slightly different approach for particle manipulation is realized by placing the tip on top of the particle during manipulation instead of placing it at the side. In this approach, which is illustrated in Fig. 17.9, the tip is first positioned approximately in the center of the nanoparticle’s top surface. If then tip motion is initiated, two scenarios are possible: (1) The tip slides over the surface of the nanoparticle with the lateral force signal reflecting the friction between tip and nanoparticle, or (2) the nanoparticle is following the tip motion by gliding over the substrate. In this case, which we will refer to as the ‘tip-on-top’ manipulation mode, the measured torsional signal is directly proportional to the interfacial friction between particle and substrate.

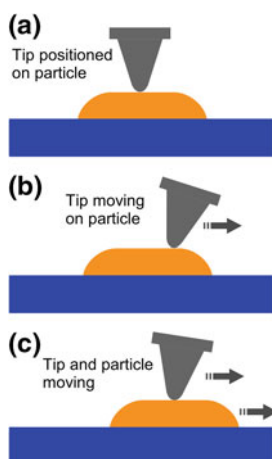


Fig. 17.9 Figure illustrating nanoparticle manipulation by employing the ‘tip-on-top’ approach described in the text. **a** *Top* The tip is positioned on top of a particle (starting position). **b** If motion of the cantilever is initiated and the cantilever normal force is below a certain threshold value, the cantilever is sliding on the particle, profiling the nanoparticle’s top surface. **c** If the cantilever load is above the threshold, the tip remains on a fixed position on top of the particle and tip and particle will move together

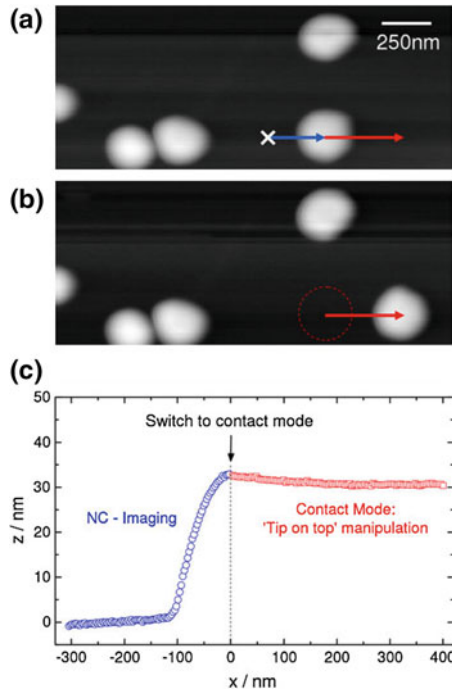


Fig. 17.10 Example of a controlled manipulation performed in the ‘tip-on-top’ mode. **a** Non-contact topography image before manipulation. The *cross* indicates the initial cantilever position, whereas the two *arrows* mark the paths used to position the cantilever on top of the particle and to perform the manipulation along the vector path. **b** Non-contact topography image after the nanoparticle manipulation along the vector path. **c** Topography signal measured during the two vector pathways. First the tip is positioned on top of the nanoparticle in noncontact mode ($x \leq 0$) and subsequently the manipulation is done in contact mode ($x \geq 0$) (figure adapted from [63])

The crucial parameter that distinguishes between the two scenarios is the ratio of the shear forces in the tip-particle-substrate system. Only if the lateral force needed to shear the tip-particle interface is larger than the force required to shear the particle-substrate interface, the particle moves together with the tip. If this is the case nanoparticles can be moved over large distances while the tip is placed on top of them. An example is given in Fig. 17.10e, where an antimony particle has been displaced under UHV conditions in the ‘tip-on-top’ mode.

One strategy to perform nanoparticle manipulations using the tip on top mode is to first operate the AFM in non-contact mode and placing the tip either on the left or right hand side of the chosen nanoparticle (Fig. 17.7a, position marked by the cross). Then the tip is first scanned across half of the particle (as indicated in Fig. 17.7a), placing it directly on top of the nanoparticle (Fig. 17.10a, c for $x = 0$). At this position the AFM is switched in situ from non-contact to contact mode [60, 63] and the cantilever normal force is slowly increased, allowing to exert a sufficient lateral

force for moving the particle. Once the normal load has been set, the tip is moved along a second vector (indicated in Fig. 17.10a) to perform the controlled nanoparticle movement. During the manipulation the topography signal and the lateral force signal are recorded. Given a flat substrate surface the topography signal remains flat over the whole pathway of the manipulation (Fig. 17.10c, $x \leq 0$), as long as the tip remains firmly on top of the nanoparticle. After the particle movement is completed, the AFM is switched back from contact to non-contact mode and a control image is recorded (Fig. 17.10b) verifying the nanoparticle's manipulation path. If the normal load is sufficient, we find that nanoparticle firmly follows the tip movements allowing controlled long-distance manipulations of over $1 \mu\text{m}$ [44].

If quantitative values for interfacial friction are to be extracted from 'tip-on-top' manipulations, one has to keep in mind that in this case a single one-directional nanoparticle manipulation lacks an absolute reference level necessary to quantify the interfacial friction. Therefore, quantitative friction data must be extracted from the forward *and* backward motion of the nanoparticle, a procedure similar to recording friction loops in conventional friction force microscopy (see Sect. 17.2.3).

17.2.3 Identifying Static Friction in Nanoparticle Manipulation Experiments

One important aspect in attaining a coherent picture of friction processes at the nanoscale is the correlation between static and sliding friction. While this difference is a well known fact for friction experiments on the macro-scale, it is less clear if or how this concept is applicable to nano- or mesoscale contacts, where stick-slip motion is considered to be the dominant process. Currently, interest is especially spurred by new concepts that take ageing of nanocontacts into account [16, 66, 67]. In many cases, nanotribological ageing effects can principally be analyzed by velocity dependent measurements [13, 16], since the stick phase during stick-slip motion can be considered as a hold time, during which contact ageing can occur. However, velocity-dependent measurements only allow to vary the hold times in a certain range. To achieve longer hold times with eventually saturated contact ageing, it might be required to suspend the sliding motion altogether and reinitiate it after the desired amount of time.

Again, the well-defined interfaces between nanoparticles and substrates can form ideal model systems to undertake nanoscale processes related to static friction. To measure the static friction of nanoparticles, different strategies have successfully been employed. One of the first examples was presented by Luethi et al., where the C_{60} nanoparticle on MoS_2 was pushed from the side and the torsion of the cantilever interacting with the nanoparticle was used as a measure of interfacial friction (see Fig. 17.4b). In this case, the static friction resulted in a high cantilever torsion that was built up right before the nanoparticle started moving [58]. Once the particle was sliding steadily, a reduced lateral force signal was measured. However, the

steep increase of the lateral force signal when the cantilever hits the particle can make it difficult to identify the exact maximum, which can be interpreted as static friction, especially if typical point densities for data acquisition are used. Moreover, the process of contact formation between the tip and the nanoparticle can influence the measurement, resulting in unreliable information about static friction.

Tripathi et al. have used tapping mode manipulation techniques to assess the temperature dependence of static friction for gold nanoclusters on HOPG [55]. By measuring the threshold of amplitude reduction, at which detachment occurs, they could quantify static friction and found that the detachment of small gold nanoclusters with diameters of about 27 nm can be described as a thermally activated process, resulting in lower detachment energies measured at higher temperatures [55].

Another possible approach to distinguish between static and sliding friction is based on the ‘tip on top’ manipulation scheme [44]. With the tip resting on top of the nanoparticles, there are two possible modes of tip and cantilever movement (see Fig. 17.9): The tip can either move on top of the nanoparticles, in which case the lateral force signal represents the friction between tip and particle, or the contact between tip and particle is firm, in which case the tip drags the particle along and the lateral force signal represents the friction between particle and substrate. The key parameter to control the sliding behavior is the cantilever normal force, which can be used to facilitate the transition between static and sliding friction. The principle scheme is depicted in figure Fig. 17.11 for an Sb nanoparticles on HOPG: First the tip is positioned on top of the nanoparticle and a contact mode scan of a small area (typically $A = 20 \text{ nm}^2$) in the center of the particle is initiated. This scan starts at a low cantilever load, in which case the lateral force between tip and particle is not sufficient to overcome the static friction between particle and substrate. By gradually increasing the cantilever load, the friction between tip and nanoparticle will increase (Fig. 17.11c), until the lateral force is finally sufficient to overcome the static friction of the nanoparticles ($t = 1.85$ in Fig. 17.11c). Now, the nanoparticles is moving together with the tip and the friction level in Fig. 17.11c (red part) represents the sliding friction of the nanoparticles, whereas the maximum of friction (at $t = 1.85$, blue curve) can be interpreted as static friction of the nanoparticles. From Fig. 17.11c it can be seen, that in case of the moving nanoparticles no further load dependence can be observed, which can be understood by assuming that the nanoparticles adhesion is much larger than any applied cantilever load. The transition of dynamic states becomes also obvious from Fig. 17.11b. Right before the transition, the friction loop is fairly wide, while the related topography signal has a considerable slope related to the shape of the particle, which is not flat. After the transition, however, the friction loop is not only significantly narrower, but also the slope in topography has vanished, since now the topography signal is related to the nanoparticle sliding on the flat HOPG substrate.

It was shown, that the transition from static to sliding friction is reproducible, meaning, that the transition from static to sliding friction can be repeated several times for the same nanoparticles. Interestingly, also the ratio between static and sliding friction seemed to be constant for several particle of the same size and a typical ratio of $F_{\text{sliding}}/F_{\text{static}} \cong 0.5$ is measured.

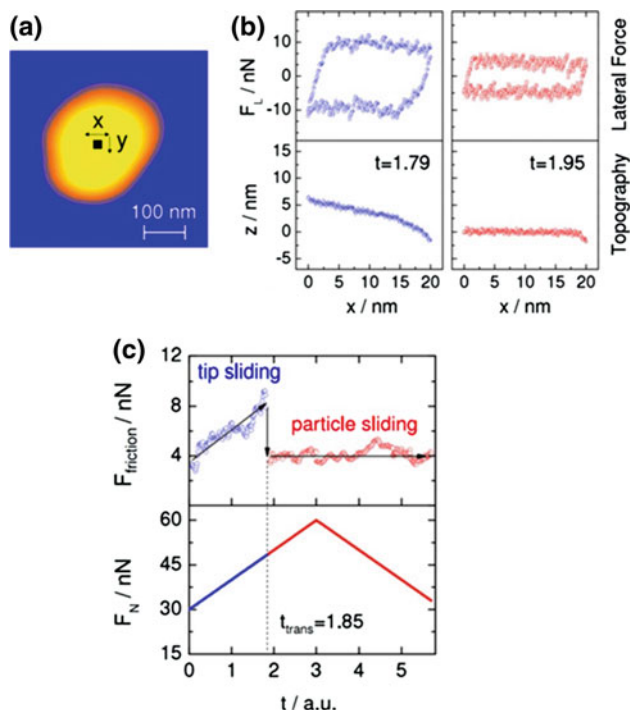


Fig. 17.11 Distiguishing static and sliding friction using the ‘tip on top’ approach. **a** Sb nanoparticle on HOPG substrate, where the typical scan area is indicated. **b** Friction loops (*top*) and topography (*bottom*) just before (*left hand panels*) and after (*right hand panels*) particle sliding was initiated. **c** Plots of the effective friction force F_{friction} and cantilever normal force F_N as a function of the time, while continuously scanning the AFM tip on top of the nanoparticle ($A_{\text{contact}} = 68,000 \text{ nm}^2$) with a scan range of $20 \text{ nm} \times 20 \text{ nm}$. The sudden drop at t_{trans} indicates the transition to particle sliding. (Figure taken from [44])

So far, the exact reason for the observed difference between static and sliding friction remains unclear. Due to the reproducibility of effects for the same nanoparticle, any wear related interface changes can be ruled out. However, theory predicts that the behavior of a layer of mobile molecules trapped between the moving surfaces can dominate the phenomenon of static and kinetic friction due to a shear force induced transition from a solidlike to a liquidlike structure of the interface layer [68]. Persson found that the ratio between kinetic and static friction is consistently one half for a wide variety of simulation parameters [68] in good agreement with the experimental results. The model also predicts that if the lateral force is reduced again, the liquidlike state prevails until much below the initial threshold, giving rise to a hysteretic behavior as observed experimentally [44]. Nonetheless, in our UHV experiments it is difficult to imagine the presence of a layer of additional interface molecules. Still, it is astonishing that the model from Persson is very consistent with the experimental observations, including a kinetic/static ratio of one half and hysteretic behavior.

This suggests that if no contamination particles are present, the last layer of Sb atoms in contact with the HOPG substrate might act as a de facto boundary lubrication layer.

17.2.4 Comparison of Manipulation Strategies

The various manipulation schemes introduced above have different advantages and drawbacks. In manipulations based on dynamic AFM modes, a high range of forces can be applied to the particles by simply adjusting the oscillation amplitude, and arbitrary translation paths for the particles can be chosen. On the downside, a direct measurement of frictional force is not possible; instead, the momentum transfer to the particle is quantified through monitoring the system's energy dissipation during manipulation. Here, it often remains unclear how much of this energy is actually transferred into the nanoparticle motion.

In contact mode manipulation, on the other hand, the fixed lateral spring constant of the specific cantilever used significantly limits the range of frictional forces that can be accurately detected. However, the restriction might be outweighed by the ability to measure the frictional force between particle and substrate directly, allowing a straightforward quantitative analysis of interfacial friction. The manipulation pathways are more limited, since friction can only be measured perpendicular to the cantilever, but in principle static and dynamic friction can be distinguished. When placing the tip on top of the particles the manipulation control is even better, since a fixed contact between nanoparticle and tip exists. In this configuration, it is possible to perform multiple nanoparticle manipulations without braking the contact between tip and sample. First experiments showed that up to 100 consecutive manipulations are possible. This opens the door for measurements regarding two fundamental key parameters in nanotribology, namely load and velocity. For load dependent measurements, the cantilever can be used to exert a varying normal load on the particle during sliding. This would allow to measure the true load dependence of friction, an issue of considerable fundamental interest. Furthermore, it is possible to vary the sliding velocity of the nanoparticle within an uninterrupted series of nanoparticle manipulations. Such experiments might clarify, how the basic model of thermal activation can be transferred from small contact areas of AFM tips to the extended contacts of nanoparticles.

17.3 Nanoparticles for Manipulation Experiments

Of course, for any nanoparticle manipulation experiments, the nanoparticles itself are of paramount importance. In principle, any mechanically stable particle that has been transferred onto a flat substrate can be investigated by AFM-based manipulation techniques. In order to investigate the frictional properties of very clean interfaces, however, it is mandatory to prepare nanoparticles under ultrahigh vacuum conditions

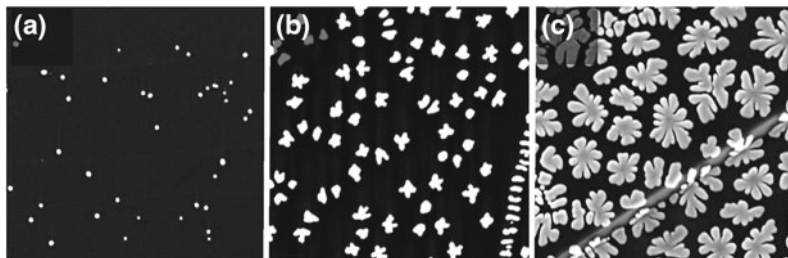


Fig. 17.12 Scanning electron microscopy images of the sample surface morphology after deposition of the equivalent of **a** 2 monolayers (ML), **b** 10 ML, and **c** 40 ML of antimony on a HOPG(0001) substrate surface at a deposition rate of 0.1 nm/s. Image size is $3.6 \times 3.6 \mu\text{m}^2$ in all cases (*images* courtesy of B. Stegemann, HTW-Berlin)

(UHV) and transfer those samples to an UHV-AFM without breaking the vacuum. One approach that achieves this goal is the in-situ thermal evaporation of metals onto a flat substrate.

An example is shown in Fig. 17.12, representing metallic antimony particles grown by thermal evaporation on highly oriented pyrolytic graphite (HOPG). The precise growth parameters and their atomic structure have been studied in detail before [69]. It was found that small, round shaped particles are amorphous, whereas particles with diameters larger than ≈ 60 nm can already be crystalline (note that the exact characteristic particle size where the transition between the two states occurs depends on the exact evaporation parameters, e.g. surface temperature or evaporation rate [70]). Since it is expected that nanoscale friction is governed by the atomistic structure of the particle-substrate interface, the occurrence of this structural transition allows for a unique study case. And indeed, Ritter et al. have recently reported on two distinct shear stresses observed during nanomanipulation experiments on antimony nanoparticles on HOPG under ambient conditions. For larger particles a shear stress three times as high as for smaller particles was found, with the contact area of transition ($A_{\text{transition}} \cong 20,000 \text{ nm}^2$) coinciding with the structural transition from compact to more branched particles [71].

Recent theoretical studies also suggest that in the case of crystalline nanoparticles, the particle orientation can be of considerable importance for the frictional behaviour of nanoparticles [33], especially due to the occurrence of commensurate and incommensurate orientation between nanoparticle and substrate. But although antimony nanoparticles become crystalline, their large size and branched structure make them inappropriate for systematic analysis of orientation dependence. A far more suitable model system is formed by gold nanoparticles on HOPG. Similar to antimony nanoparticles, gold particles can also be grown by thermal evaporation under UHV conditions, resulting in particles with clean and well defined interfaces. The crystalline structure of such gold nanoparticles is directly obvious from SEM measurements (Fig. 17.13). Topography images of the nanoparticles thus allow to directly determine the orientation of the particles, while the orientation of the

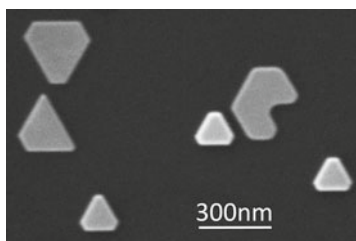


Fig. 17.13 Scanning electron microscopy image of a selection of gold nanoparticles evaporated onto freshly cleaved HOPG under UHV conditions. The evaporation time was 2 min with the gold filled crucible heated to 1380 °C while the HOPG substrate was kept at room temperature

substrate can be determined from atomically resolved stick-slip measurements in direct vicinity of the nanoparticles. The additional option to rotate the nanoparticles by off-center manipulations makes this sample system an ideal candidate to systematically analyze the directional dependence of interfacial friction in case of crystalline interfaces.

Despite the potential for the analysis of fundamental effects in interfacial friction, the approach of particle preparation by thermal evaporation is rather limited. Chemical methods can yield a much higher variety of different shapes, sizes, and surface functionalization. For example, gold particles can be prepared in very wide range of geometries, including spheres, rods, and even star-like shapes (see Fig. 17.14). Furthermore, they can be coated with self-assembled monolayers terminated with hydrophobic (e.g., methyl, $-\text{CH}_3$) or hydrophilic groups (e.g., hydroxyl, $-\text{OH}$). This allows to study the influence of the hydrophobicity of the coatings on the mobility of the nanoparticles [41]. Tranvouez et al. have studied ligand-capped cadmium selenide nanorods deposited on HOPG by AFM manipulation techniques and found a distinct anisotropy in nanoparticle movement, depending whether the rod was moved parallel or perpendicular to its main axis. These observations could then be

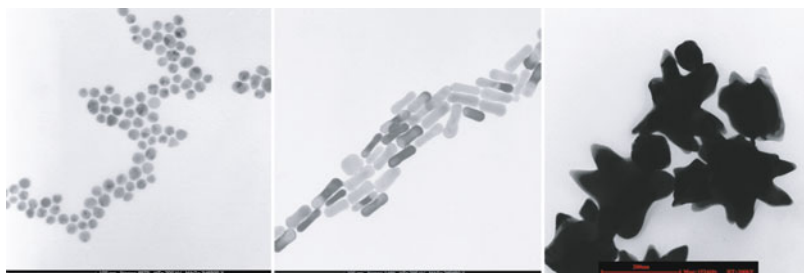


Fig. 17.14 Gold nanoparticles with different shapes suitable for manipulation experiments: *Spheres* (image size $280 \times 300 \text{ nm}^2$), *rods* (image size $370 \times 390 \text{ nm}^2$); and even complex geometries like stars can be prepared by chemical methods (image size $630 \times 650 \text{ nm}^2$, image courtesy of Karine Mougín, Institute de Science des Matériaux de Mulhouse, CNRS-LRC)

linked to the alignment between the organic ligands surrounding the nanorod and the substrate [42].

In addition to these ways of preparing nanoparticles for manipulation experiments, recent publications have shown that nanostructures suitable for manipulation experiments can also be gained from a variety of other inventive experimental strategies. For example, Bombis et al. have shown that after evaporation of NaCl on Cu(111), NaCl nanoparticles suitable for manipulation can be cut from larger NaCl structures [72]. This approach is especially interesting, since size and shape of such nanoparticles can in principle directly be controlled. Additionally, Feng et al. have reported on the mobility of graphite flakes on graphene, where the flakes have been prepared by H₂O assisted cracking of graphene sheets [73]. The results confirmed the strong dependence of interfacial friction on the relative orientation between flake and substrate, as previously reported by Dienwiebel et al. for the case of a graphite flake trapped between AFM-tip and HOPG substrate [29].

17.4 Friction of Extended Nanocontacts: Theoretical Concepts

Since the advent of friction force microscopy in 1987, most research in the field of nanotribology has concentrated on the analysis of very small contact areas, so-called nano-asperities. The interest to focus on nano-asperities was spurred because any real surface can be described as a complex system of multiple asperities, which was first recognized in the 1950's by Bowden and Tabor [74]. Experimentally, the contact between an AFM tip and a surface can be considered an ideal model system for such single asperities. In this configuration, friction force microscopy allows to analyze the basic friction processes of point contacts on the atomic scale and in most cases, the experimental results could be explained by theoretical models, which reduced the contact to only a few atoms or even a single atom [10, 13, 16]. Considerably less research has, however, been done on extended nanocontacts, even though they represent the most frequent building block of realistic surfaces in most current theories describing the contact mechanics of realistic surfaces. As a consequence, a lot of aspects of frictional behavior of extended nanocontacts are still not yet fully explored. One of the most fundamental - yet unresolved - question in current nanotribology concerns the question of how the frictional force F_{friction} experienced at a finite, atomically flat interface of nanoscopic dimensions scales with the actual contact area A_{contact} . The answer might even affect our understanding of the widely accepted classical friction laws of Amontons, who stated that friction is proportional to the normal force, but independent of the apparent contact area:

$$F_{\text{friction}} = \mu F_{\text{load}}. \quad (17.2)$$

Here F_{load} represents the external loading force and μ the friction coefficient, which depends only on the actual combination of materials in contact. Only under the assumption of a linear dependence between true contact area and friction, this

law can be understood by the commonly acknowledged model first introduced by Greenwood and Williamson [75], where a linear dependence between the real contact area between two surfaces and the applied load on the interface is assumed.

However, not only the unresolved questions regarding contact area dependence of friction make extended nanocontacts an intriguing problem. Another aspect of fundamental interest is the fact that in contrast to atomic point contacts where mostly the interaction of single atoms is considered, the collective behaviour of a multitude of atoms *within* the two surfaces sliding relative to each other can be of significant importance. The relevance of such collective behaviour becomes most obvious in the case of an effect called 'structural lubricity', which, as described below in detail, depends on the degree of interlocking between the atoms of two extended surfaces.

One key parameter determining interfacial friction between two sliders is the ratio of lattice constants. Let us first consider the case of incommensurate lattices, i.e., the lattice constants do not match. In this case, if two flat surfaces move relative to each other, on average, for every asperity or atom going up a ramp, another one is going down. As a consequence, the mean friction between rigid surfaces must vanish unless they happen to have the same periodicity and alignment. In this case, all atoms have to go up or down at the same time, resulting in a high effective energy barrier that is scaling proportional to the contact area [76]. Basically, elastic deformations of the surfaces might alter this behaviour, but detailed calculations show that elastic deformations are generally too small to modify these general conclusions [24, 77–79]. The effect of low friction due to non matching interfaces has originally been termed '*superlubricity*' [24, 80]; however, as it is a purely structural effect and to distinguish it from other effects that may lower the interfacial friction, it has been suggested by Müser to denote it more adequately as '*structural lubricity*' [25].

Figure 17.15 illustrates the situation from slightly different viewpoint. It shows the surface atoms of a substrate and the surface potential they cause. If only one atom was placed in this surface potential (Fig. 17.15I), it drops into a deep minimum and a huge energy barrier has to be overcome to displace it by one lattice constant a .

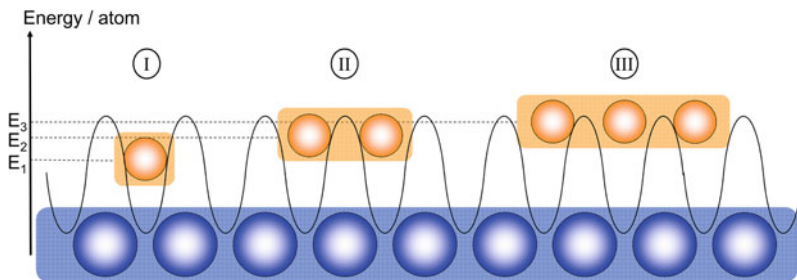


Fig. 17.15 Figure illustrating the effect of incommensurability on the average barrier between potential minima: While the number of atoms that have to overcome a barrier increases from one to three for (I) to (III), the height of the individual barriers shrinks significantly. For increasingly larger contacts, the effective overall barrier height will approach zero even though a large number of atoms contributes to the frictional resistance

However, if we placed *two* atoms in a fixed structural relation with each other on the surface, featuring a lattice constant $b \neq a$, the energy barrier that has to be overcome by each individual atom to move the entire two-atom cluster by a has shrunk considerably (Fig. 17.15II). This principle continues for increasing contact sizes (see Fig. 17.15III) and ultimately results in a vanishing energy barrier and therefore ultra-low friction as long as substrate and slider have incommensurate lattices or feature disordered (amorphous) surfaces. While it is difficult to give an analytic expression describing the case of incommensurate lattices, one can show that the static friction F_{static} between dry, amorphous, and flat surfaces depends on the contact area A with

$$F_{\text{static}} \propto F_{\text{load}}/\sqrt{A_{\text{contact}}} \quad (17.3)$$

due to the averaging effect of probability theory's central limit theorem [76].

In case of an amorphous interface structure, the contact area A_{contact} is the *only* parameter determining the scaling of interfacial friction, meaning that the interfacial friction is not affected by altering the particle's shape or orientation as long as the contact area remains constant. For crystalline interfaces, however, the situation is more complex. In recent theoretical studies, deWijn [33] has analytically calculated the friction for the case of triangular nanocrystals on a hexagonal substrate, a configuration suitable to describe, e.g., gold nanoparticles on HOPG. It is found that the scaling of friction with contact area sensitively depends on the particle's shape and orientation. For triangular particles with non-matching lattice constants, incommensurate and pseudo-commensurate orientations have been identified, which result in different power laws describing the friction versus contact area. While the friction scales $F_{\text{friction}} \propto A^0$ for incommensurate orientations, an increase of friction described by $F_{\text{friction}} \propto A^{0.5}$ is found for the pseudo-commensurate case. If irregularly shaped nanoparticles are considered, the powers can increase significantly, e.g. from 0 to 0.25 for incommensurate orientations, indicating that an irregular particle shape effectively weakens the efficiency of structural lubricity.

Currently, many aspects of structural lubricity are still under debate, such as the exact circumstances under which a superlubric state can actually be established. However, a growing number of experimental studies already seems to corroborate its existence [26–29, 35]. The results from [29] show a significant increase of the friction for relative angles between a tip and a graphite surface of about 0° and 60° , but ultra-low friction is found for all other angles. In order to explain their results, the authors assumed that the tip has picked up a small graphite flake during scanning. This flake would then be commensurate with the underlying lattice for sliding angles of 0° and 60° , but incommensurate for all angles in between.

Nonetheless, a structure-induced superlubric state still seems to be more exotic than widespread. Not only that FFM experiments have been reported where the friction-load dependence appears to be linear, but also macroscopically measured friction coefficients are always substantial and do not vanish with increasing contact area. What could be the reason that structural lubricity is so difficult to observe? According to a suggestion by He et al. [81] the problem is that realistic contacts

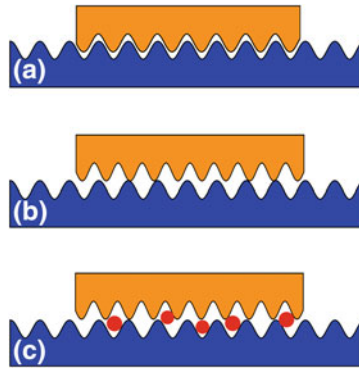


Fig. 17.16 Figure illustrating the effect of contamination on the resulting friction coefficient. **a** The atomic structure of two commensurate surfaces in contact can interlock, resulting in an area-independent friction coefficient. **b** Structural lubricity: Two incommensurate, atomically flat surfaces. The barrier between stable potential minima, and thus the friction coefficient, decreases with increasing contact size. **c** If the contact in **b**) is contaminated with mobile interface molecules, the friction coefficient is again independent of the contact size. In this case, the mobile molecules can always lock at suitable potential minima, acting as molecular mediators between the incommensurate structures

almost always feature adsorbed, but mobile molecules that are trapped between the sliding surfaces. Examples for such molecules are small hydrocarbon or water molecules that adhere on any surface (this effect can be only prevented by ultrahigh vacuum conditions). Often referred to as ‘dirt particles’, these molecules prevent a direct interaction of the surface potentials of the sliding interfaces by acting as spacers. Since their mobility allows them to simultaneously lock at surface potential minima for both sliders, an area-independent friction coefficient is obtained for any surface geometry (see Fig. 17.16). Due to the ubiquity of contamination, this effect even represents the assumed reason for the linear scaling between contact area and friction and thus for the apparent universality of Amontons’ law [76].

Another reason, that may prevent systems displaying structural lubricity, even under very clean interface conditions, may be the nature of interaction between the interfaces. If, e.g., strong chemical bonds between the interfaces are possible, the interfacial friction should depend mainly on the number of bonds. Szlufarska et al. have used MD simulations to analyze this szenario for amorphous carbon tips on diamond substrates (both terminated with hydrogen) [82] and could determine for all Si atoms at the interface whether a bond to the substrate was formed or not, which was dependent on the proximity between Si atom and substrate. In this case, the contact area is defined by the region in which bonds are build and the number of bonds determines the friction. In case of an atomically flat contact, friction should then scale proportional to the contact area with no reduction of friction related to structural lubrication effects.

When analyzing the friction of nanoparticles, it has also to be considered whether the contact area of the nanoparticle can really be considered to be completely rigid.

In a rigid configuration, a lot of fundamental characteristics regarding commensurate or incommensurate interfaces can be predicted. However, elastic deformations might change the particle's behaviour. For example, Reguzzoni et al. have used MD simulations, to describe the onset of a slip process in a Xe film on a Cu substrate [83], a system where a commensurate contact can be assumed. If an external load is applied to this system, this can result in a frictional slip that originates from the nucleation of a small commensurate domain. By this simulations, Reguzzoni et al. could understand QCM experiments results obtained by Coffey et al., where particle movement was observed in spite of an energy barrier that was definitely too high to be overcome in the absence of the nucleation of structurally distinct domains [49].

17.5 Frictional Duality of Sliding Nanoparticles

17.5.1 Contact Area Dependence of Friction Analyzed by Nanoparticle Manipulation

The above-raised fundamental questions related to the area dependence of frictional forces are ideally addressed by particle manipulation. Since crystalline or amorphous particles of different sizes can be prepared on atomically flat surfaces, a systematic assessment of friction as a function contact area is possible. This strategy was followed in two recent studies where the friction of metallic antimony particles on a flat graphite surface was studied [34, 35].

In the work of Ritter et al. [34] particles were investigated under ambient conditions at room temperature using dynamic mode AFM manipulation. In these experiments the energy dissipation at the manipulation threshold was analyzed as a function of the contact area between particle and substrate. The results for antimony particles on two different substrates, HOPG (triangles) and MoS₂ (circles), are shown in Fig. 17.17. The contact areas of the various particles range from 10,000 to 110,000 nm². The data displayed in Fig. 17.17 implies a linear relationship for the dependence of the dissipated power P_{tip} (which is equivalent to ΔE in (17.1)) on the particle's contact area with the substrate.

As outlined above, theoretical considerations suggest that for crystalline, non-commensurate surfaces in contact, friction should scale with the square root of the contact area, which is contradictory to the above results. Furthermore, an offset in the friction-size relation is observed in Fig. 17.17, which remains puzzling. However, one has to consider that there might be an influence of particle geometry on the momentum transfer of the oscillating tip to the particles. Further, these measurements were done under ambient conditions, and surface contamination may play an important role, as discussed in the previous section (see Fig. 17.16c). Therefore, we turn in the following to another set of experiments, which were performed under ultrahigh vacuum conditions to ensure clean interfaces [35]. Additionally, the experiments were carried out using the contact mode manipulation method. This yields directly

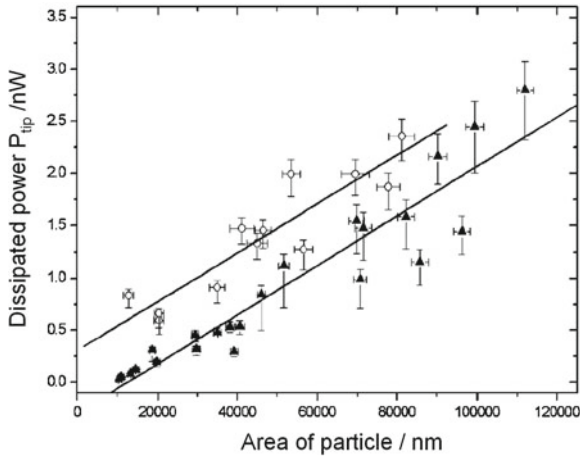


Fig. 17.17 Plot of the minimum values of power dissipation needed for translation of differently-sized Sb nanoparticles on HOPG (*filled triangles*) and MoS₂ (*empty circles*), respectively. The threshold values for both substrates are in the same range and scale linearly with the contact area of the translated particles. The *straight lines* represent linear fits of the measured data. The heights of the translated particles had an average value of 26.2 nm for the 23 particles moved on HOPG and 21.5 nm for the 12 particles moved on MoS₂ (adapted from [34])

quantitative friction values, thus avoiding possible ambiguities from the unknown impact angle in dynamic AFM manipulation.

The results of several individual dislocation events using particles featuring contact areas of up to 200,000 nm² are presented in Fig. 17.18. These events can be categorized in two distinct regimes: While the majority featured substantial frictional resistance (regime 1; solid symbols), about 1/4 of the events showed almost no detectable friction (regime 2; open symbols), causing an apparent 'frictional duality'. The results in regime 1 suggest a linear dependence and a constant shear stress $\tau = F_l/A = (1.04 \pm 0.06)$ MPa. Since the normal force experienced by the particles is due to adhesion, which scales linearly with area, an area-independent friction coefficient follows, reinforcing Amontons' law at the nanoscale.

But what is the reason for the unexpected vanishing friction behaviour of one quarter of the particles? First, we consider two possible artifacts to account for the occurrence of vanishing friction: Those particles may be picked up by the tip during translation or they may be stuck on a graphite flake that slides superlubric [29]. The pick-up hypothesis can be discarded since frictionless displaced particles could still be imaged directly after translation (see Fig. 17.19). The case of a graphite flake stuck underneath the particle is also unlikely since the images recorded after particle manipulation show no sign of missing graphite flakes. Thus, the vanishing friction behaviour must be correlated to the physical properties of the particles and/or the interface.

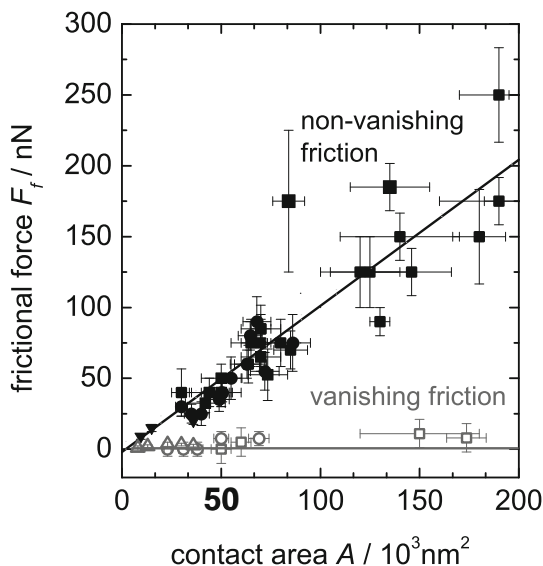


Fig. 17.18 Contact area dependence of the lateral forces experienced during nanoparticle manipulation in ultrahigh vacuum. The lateral force component of the total force is plotted versus the previously determined size of the manipulated islands, which corresponds directly to the contact area between island and substrate. Two regimes are visible: While the majority featured substantial frictional resistance (regime 1; *solid symbols*), about 1/4 of the events showed almost no detectable friction (regime 2; *open symbols*), causing an apparent ‘frictional duality’ (Figure taken from [35])

Close observation of the island structure by AFM imaging shows no systematic correlation of particle features (e.g., degree of ramification, structure, or height) with the occurrence of vanishing friction. Indeed, islands of comparable size and shape can show completely different frictional behavior within one scan frame. Also, the friction measurements show a high degree of reproducibility during multiple translation of the same particle (cf. Fig. 8 in [60]). This suggests that the properties of the particle-surface interface are decisive for the observed duality.

So what about the atomic structure of the interface? If the particles are crystalline and exhibit well-ordered, crystalline interfaces, the observation of finite friction (commensurate interfaces) or vanishing friction (incommensurate interfaces) is expected [27, 29, 80] (note that the occurrence of commensurability and incommensurability also depends on the orientation of the particle lattice relative to the substrate). The compact shape of most of the particles, however, suggests them being amorphous [69]. And even if some of the particles were crystalline, the atomic lattices of Sb and HOPG do not match, i.e., the interfaces are incommensurate under all circumstances. As a result, superlubric behavior should prevail, which is in contradiction to the observed duality.

Thus, let us recall that theoretical investigations predict superlubric behaviour to break down if small amounts of mobile molecules are trapped between the sliding

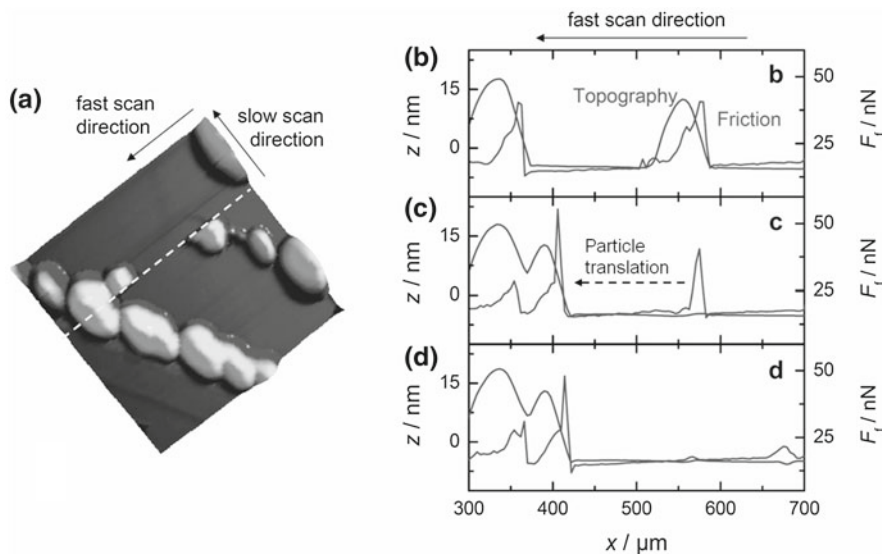


Fig. 17.19 **a** Translation event of an Sb nanoparticle with a contact area of $8\,000\text{ nm}^2$ (topography signal). **b–d** The corresponding scan lines just before (**b**), during (**c**), and right after (**d**) the translation of the particle. In contrast to Fig. 17.5e, the friction signal here only shows a peak where the tip hits the island at its initial position ($x = 580\text{ nm}$) and remains flat afterwards (below 1 nN) until the island reaches its new resting position (*Image* taken from [35])

surfaces [76, 81]. Those molecules act as mediators between the top and bottom atomic lattices and an area independent friction coefficient was found in simulations [76]. This effect seems not to depend strongly on the level of contamination [81]. In the experiments of Dietzel et al. [35] even under ‘clean’ UHV conditions, a fair number of such mobile adsorbates can accumulate on HOPG surfaces over extended measurement times. One could imagine that the interfaces of some particles are atomically clean, while others experience a break-down of superlubricity due to contamination, which would explain the observed duality of nanoparticle friction.

17.5.2 The Role of Interface Contaminations: Theoretical Calculations

Although the universal presence of interface contamination seems to be a very plausible explanation for the observed duality in friction of nanoparticles, the question remains if conceivable concentrations of likely contaminants are really sufficient to quantitatively explain the friction levels observed in nanomanipulation experiments. In order to clarify this question, Brndiar et al. used density functional (DFT)

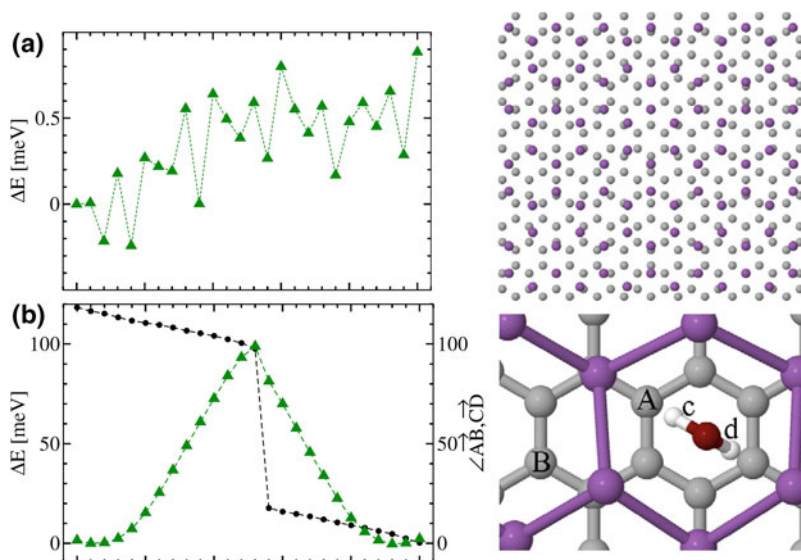


Fig. 17.20 Potential energy landscape (left panels, green triangles) calculated for a clean, crystalline Sb/HOPG interface (a) and an Sb/HOPG interface with a H_2O molecule trapped in the interface (right panels). The black spheres in (b) indicate the relative orientation between the H_2O molecule and the substrate, showing, that the trapped molecule is indeed mobile (figure adapted from [84])

modeling and analyzed the behaviour of different contamination atoms or molecules at the interface between HOPG and crystalline antimony [84]. By calculating the potential energy surface (PES) for the sliding process with and without contaminants, information could be gained about the additional energy barriers that need to be overcome in the presence of contaminants. Figure 17.20 illustrates the results for the case of a clean interface and an interface with an H_2O molecule trapped between the surfaces of 2.6 nm^2 size. While the clean interface results in a very low energy barrier ($E_{\text{barrier}} < 1 \text{ meV}$), which is consistent with the expectations for structural lubricity, adding an H_2O molecule into the interface results in a substantial increase of the energy barrier, which is found to be approximately 100 meV. Similar effects and energy barriers were found when adding an Sb_4 -clusters or one oxygen atom or Sb_4O_6 into the interface.

The simulations by Brndiar et al. revealed that the trapped H_2O molecule is moving along with the antimony surface, but still remains essentially mobile. This mobility is indicated in Fig. 17.20b, where the rotation of H_2O molecule during translation is plotted. Particle mobility is an important condition for ‘dirt’ molecules to function as mediators between incommensurate interfaces [76]. If dirt molecules would be fixed and rigidly bound to, e.g., the particle, the resulting new interface would again show superlubricity.

In an attempt to estimate the number of contamination molecules at the interfaces, it was found, that approximately 1 H₂O molecule/75 nm² is required to explain the experimentally observed friction levels. This value seems to be conceivable, especially, when considering, that the HOPG used for experiments was cleaved under ambient conditions [35]. On the other hand, a concentration of 1 Sb₄/7 nm² was found to be required. While this concentration in itself seems to be very high, it might be understood by assuming that Sb₄ clusters loosely attached to the sliding surface of the particle might act as self contaminants. In any case, these simulations affirm the plausibility of interface contamination to be responsible for the observed frictional duality.

17.6 Conclusion and Outlook

In recent years, analyzing friction by nanoparticle manipulation has become a field of growing interest in nanotribology. The quantitative extraction of interfacial friction from particle manipulation experiments opens the door for the analysis of many current issues in the field of nanoscale friction. Compared to conventional friction force microscopy, the accessible range of materials is greatly enhanced and only limited by the ability to create nanoscale particles on flat surfaces. Due to the well defined and clean interface conditions that can be achieved during nanoparticle manipulation experiments under UHV conditions, it is possible to verify fundamental tribological theories describing the friction between extended nanocontacts. Most prominently, the contact area dependence of friction can be analyzed in detail, which was previously hindered by the geometric limitations of tip-sample contacts in conventional friction force microscopy. Experiments show that such measurements are also suitable to approach other current issues in nanotribology like the occurrence of structural lubricity and the influence of interface contamination on friction.

Over the years, different experimental strategies have evolved, the choice of which mostly depends on the experimental conditions or the nanoparticles to be analyzed. Nowadays, especially the 'tip on top'-approach seems to be very promising for the analysis of fundamental friction processes. It was initially introduced to measure the difference between static and sliding friction, but the permanent contact between tip and nanoparticle also makes it an interesting approach to perform systematic measurements with, e.g., variation of the normal force or sliding velocity. Through this approach, it can be analyzed how fundamental concepts describing atomic friction, such as the thermally activated Prandtl-Thomlinson-Model, can be transferred to extended nanocontacts.

Furthermore, the analysis of friction by nanoparticle manipulations is not only interesting for analyzing fundamental friction laws, but can also be relevant for technological applications. Compared to conventional friction force microscopy with contact sizes of about 10–100 nm², nanoparticle manipulation allows the analysis of far more realistic contact sizes that can also be found in micro- or nanoelectromechanical systems (MEMS, NEMS), where friction and wear currently still

limit the perspective for widespread application. Understanding friction for such mesoscale contacts might therefore have a considerable impact on technological applications.

Acknowledgments U.S. acknowledges primary financial support by the National Science Foundation through the Yale Materials Research Science and Engineering Center (Grant No. MRSEC DMR-1119826).

References

1. M. Mate, G.M. McClelland, R. Erlandsson, S. Chiang, *Phys. Rev. Lett.* **59**, 1942–1945 (1987)
2. E. Gnecco, E. Meyer (eds.), *Fundamentals of Friction and Wear on the Nanoscale* (Springer, Berlin, 2007)
3. R.W. Carpick, M. Salmeron, *Chem. Rev.* **97**, 1163 (1997)
4. R.W. Carpick, N. Agrait, D.F. Ogletree, M. Salmeron, *J. Vac. Sci. Technol. B* **14**, 1289 (1996)
5. M.A. Lantz, S.J. O’Shea, M.E. Welland, K.L. Johnson, *Phys. Rev. B* **1997**(55), 10776 (1997)
6. U.D. Schwarz, O. Zwörner, P. Köster, R. Wiesendanger, *Phys. Rev. B* **56**, 6987 (1997)
7. U.D. Schwarz, O. Zwörner, P. Köster, R. Wiesendanger, *Phys. Rev. B* **56**, 6997 (1997)
8. E. Meyer, R. Lüthi, L. Howald, M. Bammerlin, M. Guggisberg, H.-J. Güntherodt, *J. Vac. Sci. Technol. B* **14**, 1285 (1996)
9. M. Enachescu, R.J.A. van den Oetelaar, R.W. Carpick, D.F. Ogletree, C.F.J. Flipse, M. Salmeron, *Phys. Rev. Lett.* **1998**, 81 (1877)
10. E. Gnecco, R. Bennewitz, T. Gyalog, Ch. Loppacher, M. Bammerlin, E. Meyer, H.-J. Güntherodt, *Phys. Rev. Lett.* **84**, 1172–1175 (2000)
11. M. Evstigneev, A. Schirmeisen, L. Jansen, H. Fuchs, P. Reimann, *Phys. Rev. Lett.* **97**, 240601 (2006)
12. O. Zwörner, H. Hölscher, U.D. Schwarz, R. Wiesendanger, *Appl. Phys. A* **66**, S263 (1998)
13. L. Jansen, H. Hölscher, H. Fuchs, A. Schirmeisen, *Phys. Rev. Lett.* **104**, 256101 (2010)
14. A. Schirmeisen, L. Jansen, H. Hölscher, H. Fuchs, *Appl. Phys. Lett.* **88**, 123108 (2006)
15. X. Zhao, M. Hamilton, W.G. Sawyer, S.S. Perry, *Trib. Lett.* **27**, 113 (2007)
16. I. Barel, M. Urbakh, L. Jansen, A. Schirmeisen, *Phys. Rev. Lett.* **104**, 066104 (2010)
17. R.M. Overney, H. Takano, M. Fujihira, W. Paulus, H. Ringsdorf, *Phys. Rev. Lett.* **72**, 3546 (1994)
18. H. Bluhm, U.D. Schwarz, K.-P. Meyer, R. Wiesendanger, *Appl. Phys. A* **61**, 525 (1995)
19. H. Shindo, K. Shitagami, T. Sugai, S.-I. Kondo, *Phys. Chem. Chem. Phys.* **1**, 1597 (1999)
20. J.Y. Park, D.F. Ogletree, M. Salmeron, R.A. Ribeiro, P.C. Canfield, C.J. Jenks, P.A. Thiel, *Science* **309**, 1354 (2005)
21. E. Meyer, R. Overney, D. Brodbeck, L. Howald, R. Lüthi, J. Frommer, H.-J. Güntherodt, *Phys. Rev. Lett.* **69**, 1777 (1992)
22. R.M. Overney, E. Meyer, J. Frommer, D. Brodbeck, R. Lüthi, L. Howald, H.-J. Güntherodt, M. Fujihira, H. Takano, Y. Gotoh, *Nature* **359**, 133 (1992)
23. U.D. Schwarz, W. Allers, G. Gensterblum, R. Wiesendanger, *Phys. Rev. B* **52**, 14976 (1995)
24. M. Hirano, K. Shinjo, *Phys. Rev. B* **41**, 11837 (1990)
25. M.H. Müser, *Europhys. Lett.* **66**, 97 (2004)
26. J.M. Martin, C. Donnet, T.L. Mogne, T. Epicier, *Phys. Rev. B* **48**, 10583 (1993)
27. M. Hirano, K. Shinjo, R. Kaneko, Y. Murata, *Phys. Rev. Lett.* **78**, 1448 (1997)
28. A. Crossley, E.H. Kisi, J.W.B. Summers, S. Myhra, *J. Phys. D* **32**, 632 (1999)
29. M. Dienwiebel, G.S. Verhoeven, N. Pradeep, J.W.M. Frenken, J.A. Heimberg, H.W. Zandbergen, *Phys. Rev. Lett.* **92**, 126101 (2004)
30. J.N. Israelachvili, *J. Colloid Interface Sci.* **44**, 259 (1973)

31. A.M. Homola, J.N. Israelachvili, P.M. McGuiggan, M.L. Gee, *Wear* **136**, 65 (1990)
32. U.D. Schwarz, *J. Colloid Interface Sci.* **261**, 99 (2003)
33. A.S. de Wijn, *Phys. Rev. B* **86**, 085429 (2012)
34. C. Ritter, M. Heyde, B. Stegemann, K. Rademann, U.D. Schwarz, *Phys. Rev. B* **71**, 085405 (2005)
35. D. Dietzel, C. Ritter, T. Mönninghoff, H. Fuchs, A. Schirmeisen, U.D. Schwarz, *Phys. Rev. Lett.* **101**, 125505 (2008)
36. A. Schirmeisen, U.D. Schwarz, *Chem. Phys. Chem* **10**, 2373 (2009)
37. R. Lüthi, E. Meyer, H. Haefke, L. Howald, W. Gutmannsbauer, H.-J. Güntherodt, *Science* **194**, 266 (1979)
38. P.E. Sheehan, C.M. Lieber, *Science* **272**, 1158 (1996)
39. M.R. Falvo, J. Steele, R.M. Taylor II, R. Superfine, *Phys. Rev. B* **62**, R10665 (2000)
40. A. Rao, E. Gnecco, D. Marchetto, K. Mougín, M. Schönenberger, S. Valeri, E. Meyer, *Nanotechnology* **20**, 115706 (2009)
41. K. Mougín, E. Gnecco, A. Rao, M.T. Cuberes, S. Jayaraman, E.W. McFarland, H. Haidara, E. Meyer, *Langmuir* **24**, 1577 (2008)
42. E. Tranvouez, A. Orioux, E. Boer-Duchemin, C.H. Devillers, V. Huc, G. Comtet, G. Dujardin, *Nanotechnology* **20**, 165304 (2009)
43. G. Paolicelli, M. Rovatti, A. Vanossi, S. Valeri, *Appl. Phys. Lett.* **95**, 143121 (2009)
44. D. Dietzel, M. Feldmann, H. Fuchs, U.D. Schwarz, A. Schirmeisen, *Appl. Phys. Lett.* **95**, 053104 (2009)
45. J.N. Israelachvili, D. Tabor, *Wear* **24**, 386–390 (1972)
46. B.J. Briscoe, D.C.B. Evans, *Proc. Roy. Soc. Lond. A* **1982**(380), 389 (1982)
47. J. Krim, A. Widom, *Phys. Rev. B* **38**, 12184–9 (1988)
48. J. Krim, D.H. Solina, R. Chiarello, *Phys. Rev. Lett.* **66**, 181–184 (1991)
49. T. Coffey, J. Krim, *Phys. Rev. Lett.* **95**, 076101 (2005)
50. Q. Zhong, D. Inniss, K. Kjoller, V. Elings, *Surf. Sci. Lett.* **290**, L688 (1993)
51. T.R. Albrecht, P. Grtter, D. Horne, D. Rugar, *J. Appl. Phys.* **69**, 668 (1991)
52. B. Anczykowski, B. Gotsmann, H. Fuchs, J.P. Cleveland, V.B. Elings, *Appl. Surf. Sci.* **140**, 376–382 (1999)
53. C. Ritter, M. Heyde, U.D. Schwarz, K. Rademann, *Langmuir* **18**, 7798–7803 (2002)
54. D.A. Aruliah, M. Müser, U.D. Schwarz, *Phys. Rev. B* **71**, 085406 (2005)
55. M. Tripathi, G. Paolicelli, S. D'Addato, S. Valeri, *Nanotechnology* **23**, 245706 (2012)
56. M. Ternes, C.P. Lutz, C.F. Hirjibehedin, F.J. Giessibl, A.J. Heinrich, *Science* **319**, 1066 (2008)
57. G. Langewisch, J. Falter, H. Fuchs, A. Schirmeisen, *Phys. Rev. Lett.* **110**, 036101 (2013)
58. R. Lüthi, E. Meyer, H. Haefke, L. Howald, W. Gutmannsbauer, H.-J. Güntherodt, *Science* **266**, 1979 (1994)
59. M. Palacio, B. Bhushan, *Nanotechnology* **19**, 315710 (2008)
60. D. Dietzel, T. Mönninghoff, L. Jansen, H. Fuchs, C. Ritter, U.D. Schwarz, A. Schirmeisen, *J. Appl. Phys.* **102**, 084306 (2007)
61. H. Ueyama, Y. Sugawara, S. Morita, *Appl. Phys. A Mater. Sci. Process.* **66**, 295 (1998)
62. A. Schirmeisen, H. Hölscher, B. Anczykowski, D. Weiner, M.M. Schäfer, H. Fuchs, *Nanotechnology* **16**, S13 (2005)
63. D. Dietzel et al., *Trib. Lett.* **39**, 273 (2010)
64. A. Rao, M.L. Wille, E. Gnecco, K. Mougín, E. Meyer, *Phys. Rev. B* **80**, 193405 (2009)
65. P. Nita, S. Casado, D. Dietzel, A. Schirmeisen, E. Gnecco, *Nanotechnology* **24**, 325302 (2013)
66. Y. Liu, I. Szlufarska, *Phys. Rev. Lett.* **109**, 186102 (2012)
67. Q. Li, T.E. Tullis, D.L. Goldsby, R.W. Carpick, *Nature* **480**, 233 (2011)
68. B.N.J. Persson, *Phys. Rev. Lett.* **71**, 1212 (1993)
69. B. Stegemann, C. Ritter, B. Kaiser, K. Rademann, *J. Phys. Chem. B* **108**, 14292 (2004)
70. B. Kaiser, B. Stegemann, H. Kaukel, K. Rademann, *Surf. Sci.* **496**, L18–L22 (2002)
71. C. Ritter, M.Z. Baykara, B. Stegemann, M. Heyde, K. Rademann, J. Schroers, U.D. Schwarz, *Phys. Rev. B* **88**, 045422 (2013)

72. C. Bombis, F. Ample, J. Mielke, M. Mannsberger, C.J. Villagmez, C. Roth, C. Joachim, L. Grill, *Phys. Rev. Lett.* **104**, 185502 (2010)
73. X. Feng, S. Kwon, J.Y. Park, M. Salmeron, *ACS Nano* **7**, 1718 (2013)
74. F.P. Bowden, D. Tabor, *The Friction and Lubrication of Solids* (Oxford University Press, New York, 1950)
75. J.A. Greenwood, J.B.P. Williamson, *Proc. R. Soc. Lond. A* **295**, 300 (1966)
76. M.H. Müser, L. Wenning, M.O. Robbins, *Phys. Rev. Lett.* **86**, 1295 (2001)
77. M. Hirano, K. Shinjo, *Wear* **168**, 121–125 (1993)
78. M.R. Sørensen, K.W. Jacobsen, P. Stoltze, *Phys. Rev. B* **53**, 2101–2113 (1996)
79. M.H. Müser, M.O. Robbins, *Phys. Rev. B* **61**, 2335–2342 (2000)
80. K. Shinjo, M. Hirano, *Surf. Sci.* **283**, 473 (1993)
81. G. He, M.H. Müser, M.O. Robbins, *Science* **284**, 1650 (1999)
82. Y. Mo, K.T. Turner, I. Szlufarska, *Nature* **457**, 1116 (2009)
83. M. Reguzzonia, M. Ferrarioa, S. Zapperia, M.C. Righia, *PNAS* **107**, 1313 (2010)
84. J. Brndiar, R. Turansky, D. Dietzel, A. Schirmeisen, I. Stich, *Nanotechnology* **22**, 085704 (2011)